Available online at www.sciencedirect.com
ScienceDirect
Trans. Nonferrous Met. Soc. China 33(2023) 2461−2470
Transactions of Nonferrous Metals Society of China
www.tnmsc.cn

Microstructural stability and mechanical properties of BCC-based $Fe_{3.5}Cr_{1.5}NiAl_{0.8}$ multicomponent alloy

Guo-jia ZHANG[1,2], Ming-liang WANG[1], Yi-ping LU[1,2], Tong-min WANG[1,2], Ting-ju LI[1]

1. Liaoning Key Laboratory of Solidification Control and Digital Preparation Technology, School of Materials Science and Engineering, Dalian University of Technology, Dalian 116024, China;
2. Liaoning Engineering Research Center of High-entropy Alloy Materials, School of Materials Science and Engineering, Dalian University of Technology, Dalian 116024, China

Received 22 February 2022; accepted 15 April 2022

Abstract: The effect of temperature on the microstructural stability and mechanical properties of ordered ellipsoidal *B*2-NiAl nanoprecipitates in a novel body-centered-cubic (BCC)-based $Fe_{3.5}Cr_{1.5}NiA_{l0.8}$ multicomponent alloy (MCA) was investigated. XRD, EBSD, EPMA and TEM were used to characterize the microstructure and phase composition of this MCA. The results showed that the designed coherent microstructure with a high-content ellipsoidal *B*2 nanoprecipitates in BCC matrix could be maintained up to a high temperature of 1073 K with an average particle size of 245.509−251.328 nm. The unique coherent structure of the as-cast and heat-treated (873 K ≤ T ≤ 1073 K) alloys could be designed to provide a high yield strength (809.2−1164.1 MPa) owing to the low-misfit coherent precipitation strengthening mechanism. When heat treatment temperature was further increased (1173 K ≤ T ≤ 1273 K), the mean particle size of the *B*2 nanoprecipitates gradually coarsened, and the load transfer strengthening mechanism played a major role in improving the yield strength.

Key words: multicomponent alloy; coherent microstructure; microstructural evolution; mechanical properties; strengthening mechanism

1 Introduction

High-entropy alloys (HEAs) or multi-component alloys (MCAs) have received considerable interest for their unique chemical, physical, and mechanical properties, and have become a hot spot in the field of metal alloy research [1−4]. HEAs generally contain five or more elements with equimolar, near-equimolar, or non-equimolar mixing, resulting in the formation of simple solid solution structures, such as face-centered-cubic (FCC), body-centered-cubic (BCC), and hexagonal close-packed (HCP) [5−7]. Recent research has revealed that single structured HEAs/MCAs are still challenging to simultaneously achieve both high strength and maintain reliable ductility [8−11].

Precipitation strengthening, especially coherent precipitation strengthening, can profoundly strengthen the solid-solution matrix and reduce plastic loss due to the low lattice misfit between the coherent ordered precipitates and solid-solution phase [12−15]. For instance, JIANG et al [1] proposed a counterintuitive strategy for designing ultrastrong steel alloys by high-density nano-precipitation and minimal lattice misfit, with a strength of up to 2.2 GPa and good ductility (about 8.2%). Owing to these highly dispersed, fully coherent precipitates, the strengthened alloys show very low lattice misfit with the surrounding matrix and high antiphase boundary energy without

Corresponding author: Ming-liang WANG, Tel: +86-13206431096, E-mail: wml_8778@163.com;
Yi-ping LU, Tel: +86-411-84709400, E-mail: luyiping@dlut.edu.cn
DOI: 10.1016/S1003-6326(23)66273-9

sacrificing the ductility. Recently, the precipitation strengthening mechanism has been applied to HEAs/MCAs to trade off the strength and ductility [16−19]. Previous research analysis has revealed that controllably introducing high-density ductile nanoparticles is also an effective method of improving the comprehensive mechanical properties in complex alloy systems. Moreover, different from the conventional wisdom of intermetallic-induced brittleness, such nanoparticle-strengthened alloys exhibit an ultrahigh strength (1.5 GPa) while retaining good ductility (~50%) in tension at ambient temperature [3]. Interestingly, dispersively distributed nanoscale BCC precipitates were also observed in a lightweight refractory $AlMo_{0.5}NbTa_{0.5}TiZr$ HEA with a *B*2-based matrix, and the nanoscale precipitates had a good coherent relationship with the matrix [20]. In addition, Al is an important element to regulate the transition from FCC-based alloy to BCC-based alloy for the improvement of strength [21]. However, the wavy microstructure formed by the BCC phase and the *B*2 phase has been found to dramatically deteriorate the plasticity of the AlNiCoFeCr alloy. Thus, the type of the substrate material and the coherently-precipitated particles are critical to strengthen the material meanwhile maintain enough ductility [22−25].

In the present study, to achieve excellent comprehensive mechanical properties, a novel Fe-based MCA was designed, which could induce the formation of a low-misfit NiAl-type *B*2 coherent nanoprecipitates into the BCC matrix, and the effects of heat treatment at different temperatures on both the mechanical properties and the precipitation behavior were investigated. In particular, the strengthening mechanism and the microstructure of these nanoprecipitates at different treatment temperatures were also addressed. This study not only offered a further understanding of the nature of precipitation hardening in MCAs but also assisted in designing MCAs with excellent mechanical properties.

2 Experimental

Master $Fe_{3.5}Cr_{1.5}NiAl_{0.8}$ MCAs (elements in atomic ratios) were prepared in nonconsumable vacuum arc melting furnace. The purity of the raw materials (Fe, Cr, Ni, and Al elements) was higher than 99.9 wt.% and remelted at least five times to ensure chemical homogeneity. The as-cast ingots were button-shaped, about 12 mm in thickness and 32 mm in diameter, and then heat-treated at 873, 973, 1073, 1173, and 1273 K for 2 h, respectively, followed by water-quenching.

The phase structure of $Fe_{3.5}Cr_{1.5}NiAl_{0.8}$ MCAs was performed by X-ray diffraction (XRD) using an EMPYREAN diffractometer with Cu K_α radiation operating at 45 kV and 40 mA and a scanning rate of 4 (°)/min in the 2θ range of 20°−100°. Electron backscatter diffraction (EBSD, Bruker eFlashHR) analyses were performed using a Zeiss supra 55 scanning electron microscope, and a step size of 0.5 μm was used to generate the EBSD maps. Microstructural characterization was carried out using an electron probe microanalyzer (JXA−8530F) and a JEM−F200 transmission electron microscope (TEM) equipped with a selected phase electron diffraction (SAED), and the chemical composition was identified with an attached energy-dispersive spectrometer (EDS). The TEM specimens were firstly mechanically ground to 35 μm in thickness, then punched into foils with a diameter of 4 mm, and finally thinned by a twin-jet electropolisher using the electrolyte contained 10 vol.% perchloric acid and 90 vol.% alcohol at a voltage of 20 kV. The hardness of the specimens was measured under a 500 g load that was applied for 15 s using an MH−50 Vickers hardness tester. Each specimen can obtain 6 indentations at equal interval of 0.4 mm and the average value of them is regarded as the hardness value. The room-temperature compressive test was performed using a DNS−100 universal testing machine, and the loading rate of the test was 1×10^{-3} s^{-1}. The cylindrical specimens had a diameter of 5 mm and a height of 10 mm.

3 Results

3.1 Microstructural characteristics

The XRD patterns of the as-cast and different heat-treated $Fe_{3.5}Cr_{1.5}NiAl_{0.8}$ MCAs are shown in Fig. 1(a), which exhibited a dual-phase structure of the BCC phase plus the *B*2 phase. In addition, a minor (100) reflection peak emerged, which was identified as the ordered *B*2 phase. Further, the lattice constants of both the BCC and *B*2 phases were a_{BCC}=0.2876 Å and a_{B2}=0.2888 Å, respectively, calculated through the $(110)_{BCC/B2}$

diffraction peak. However, the XRD patterns indicate that the $(110)_{BCC/B2}$ diffraction peak intensities decrease after aging, and the minor $(220)_{BCC/B2}$ diffraction peaks are not found in the alloys heat-treated at 1173 and 1273 K, which can be ascribed to the decrease of the volume fraction of precipitate phases. The thermodynamic calculation of the phase diagram (CALPHAD) of the MCAs was analyzed using the JMATPro software (Fig. 1(b)), which revealed the phase constitutions and fractions with temperature during solidification. The liquid phase line gradually decreased, and the primary phases were found to be the BCC phase. The ordered *B*2 phase was formed after the solidification and no other phases were found.

Figure 2 shows the grain size, morphology and distribution of the nanoprecipitate phases of the $Fe_{3.5}Cr_{1.5}NiAl_{0.8}$ MCAs. From the EBSD inverse pole figure map, it was found that all specimens

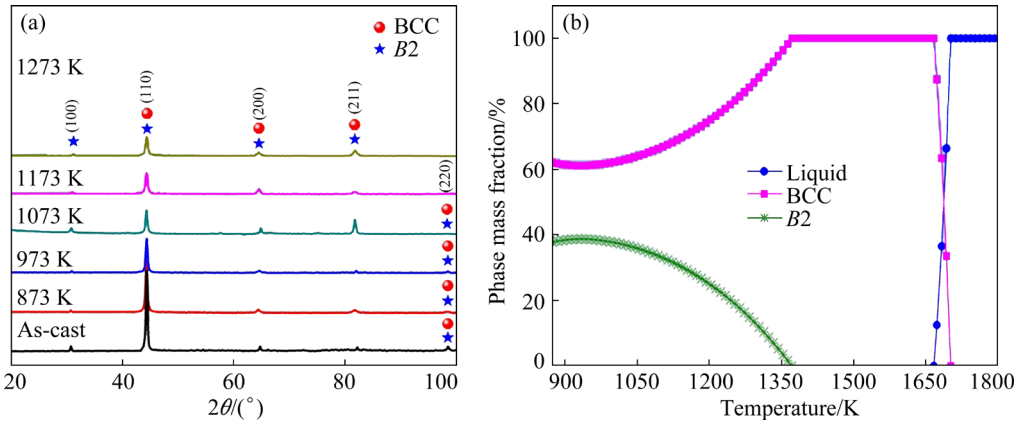

Fig. 1 XRD patterns of as-cast and different heat-treated $Fe_{3.5}Cr_{1.5}NiAl_{0.8}$ MCAs (a) and thermodynamic analysis results of solidification path of $Fe_{3.5}Cr_{1.5}NiAl_{0.8}$ MCAs by JMATPro software (b)

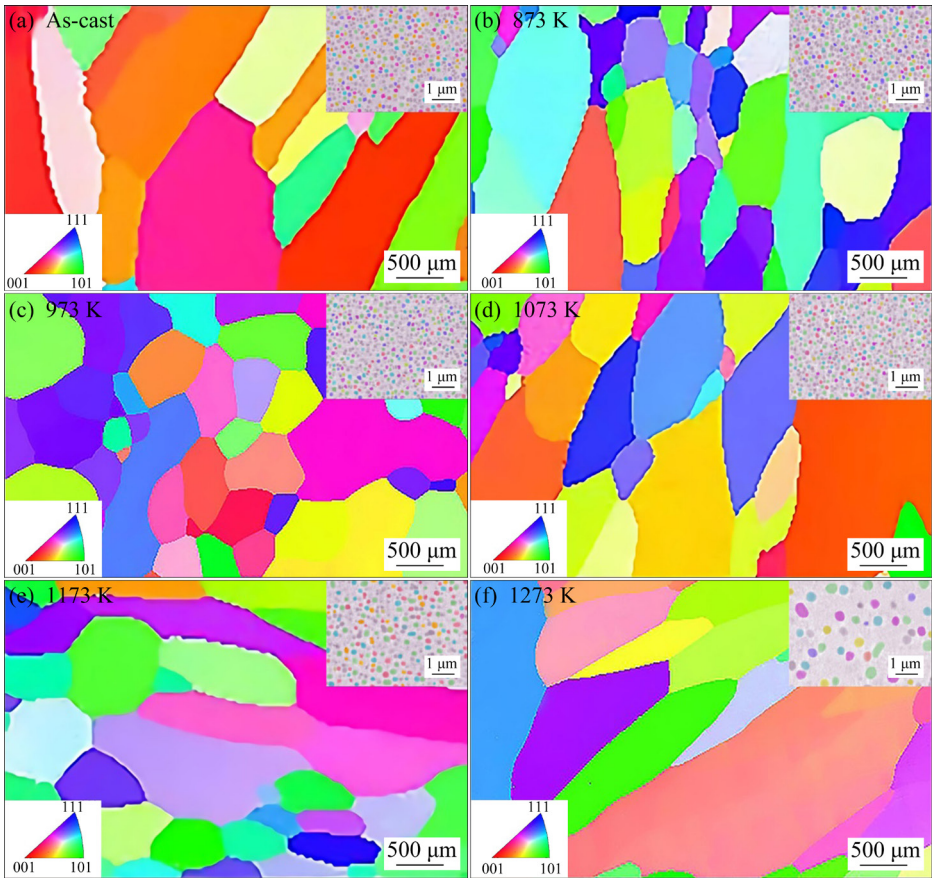

Fig. 2 EBSD micrographs of as-cast and heat-treated $Fe_{3.5}Cr_{1.5}NiAl_{0.8}$ MCAs at different temperatures (873−1273 K) for 2 h, with insets showing corresponding EPMA images

showed randomly oriented grains. The grains had an average grain size of several hundred micrometers (>500 μm) for the as-cast MCA sample. Subsequently, the alloy was subjected to isothermal heat treatment at different temperatures. The grain was gradually refined with a nonuniform size distribution, and the average grain size of the alloy was ~420.5 μm after the heating treatments at 873 and 973 K. However, after annealing at 1073, 1173, and 1273 K, the grains were elongated up to several hundred micrometers (>500 μm), which were remarkably larger than those achieved at low-temperature heat treatments. In alloys that were as-cast and heat-treated below 1073 K, the nanoprecipitates were uniformly distributed into the matrix with an average particle size of 245.509 nm at as-cast state, 246.146 nm at 873 K, 248.424 nm at 973 K, and 251.328 nm at 1073 K, as shown in Fig. 2. When the heat-treatment temperature continued to increase to 1173 and 1273 K, a drastic change was observed in the microstructure: the nanoprecipitate phases were coarsened with an average size of about 323.425 nm at 1173 K and 650.263 nm at 1273 K, and the volume fraction of the precipitates decreased, which was consistent with the thermodynamic phase diagram analysis.

A bright-field TEM image of $Fe_{3.5}Cr_{1.5}NiAl_{0.8}$ MCAs with the incident electron beam parallel to the [001] zone axis of sample grains is presented in Fig. 3. Nanoprecipitate particles with high volume fraction were uniformly distributed in the matrix, as shown in Fig. 3(a). Based on the results of the XRD analysis and thermodynamic calculations, the MCAs were composed of a *B*2 and BCC dual-phase structure. SAED pattern further verified their structures. The primary diffraction spots demonstrated that the matrix was indeed a BCC structure, whereas additional weak spots observed in the image confirmed the precipitates with a *B*2 structure. Moreover, to further observe the interfaces between nanoprecipitates and matrix in the as-cast alloy (red dashed line), high-resolution TEM (HRTEM) was employed. A coherent interface was observed between the nanoparticles

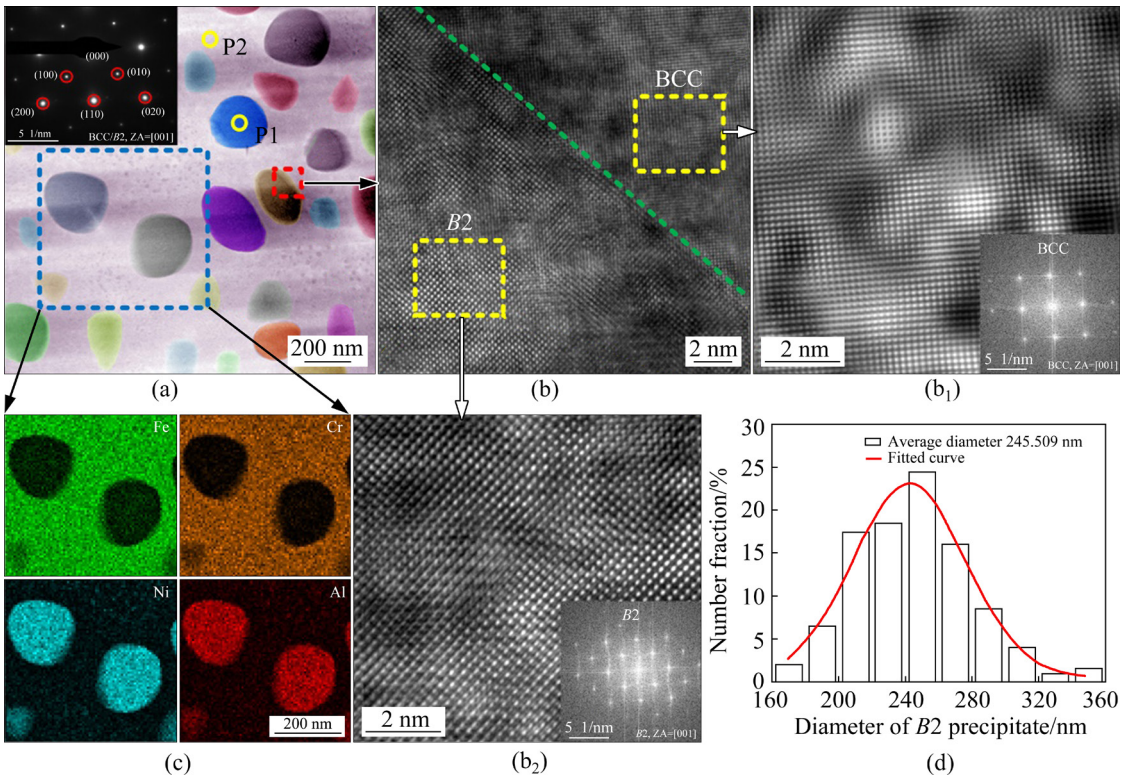

Fig. 3 Morphology, composition, size of particles, and structure of phases of as-cast $Fe_{3.5}Cr_{1.5}NiAl_{0.8}$ MCAs: (a) Bright-field TEM image of *B*2 particle and BCC matrix and corresponding SAED pattern of BCC/*B*2 phase; (b) HRTEM image revealing distinctive nanostructure consisting of *B*2 particle and BCC matrix with coherent interfaces marked with red square in (a), in which IFFT and FFT patterns obtained from BCC matrix (b_1) and *B*2 particle (b_2) are also given; (c) Elemental distributions of nanoprecipitates mapped with EDS; (d) Frequency distribution histogram corresponding to as-cast alloy in Fig. 2 showing size of nanoprecipitates

and matrix (green dashed line), which is given in Fig. 3(b). Inverse fast Fourier transform (IFFT) and fast Fourier transform (FFT) patterns were derived from the BCC matrix (Fig. 3(b_1)) and the *B*2 nanoparticles (Fig. 3(b_2)) (yellow dashed line). In addition, the chemical distribution of each element of the as-cast alloy was also mapped by the EDS (blue dashed line), as shown in Fig. 3(c). Obviously, the BCC matrix was still preferably enriched with Fe and Cr elements, while the coherent *B*2 nanoprecipitates were enriched with Ni and Al elements. The results of EDS are summarized in Table 1. The precipitate diameter distribution map corresponding to the as-cast alloy in Fig. 2 is presented in Fig. 3(d). The average diameter of the precipitate was measured to be 245.509 nm.

3.2 Mechanical properties

At different temperatures, $Fe_{3.5}Cr_{1.5}NiAl_{0.8}$ MCAs exhibited a combination of high yield strength and high hardness, as shown in Fig. 4. The yield strength of the as-cast sample was ~1164.1 MPa. With the increase in annealing temperature, the yield strength of alloys decreased continuously to 1116.3, 895.9, and 809.2 MPa at 873, 973, and 1073 K, respectively. Nevertheless, the yield strength of the alloys at an annealing temperature of 1173 K was ~1155.3 MPa. On the contrary, the alloys at an annealing temperature of 1273 K displayed the highest yield strength of ~1281.8 MPa, which was about 1.58 times as high as that of the alloys at an annealing temperature of 1073 K. With an increase in the annealing temperature, the Vickers hardness decreased from HV 416.3 to HV 329.9 when the heating temperature was not higher than 1073 K. However, the Vickers hardness of the alloy rapidly increased to HV 466.6 when the heating temperature was 1273 K, which was about 1.41 times as high as that of the alloy at a heating temperature of 1073 K. The relationships between the average Vickers hardness, the yield strength and heat treatment temperature are shown in Fig. 4(b) and Table 2. Meanwhile, it was noteworthy that the elongation of the alloys with different annealing temperatures still remained at high levels owing to the strengthening of coherent *B*2 nanoprecipitates in the BCC matrix [26−29].

4 Discussion

According to the strengthening mechanism of traditional polycrystalline alloys, the yield strength (σ_y) mainly originated from the intrinsic strength (σ_0), the solid-solution strengthening ($\Delta\sigma_{ss}$), the grain-boundary strengthening ($\Delta\sigma_{gb}$), the dislocation strengthening ($\Delta\sigma_{dis}$), and the precipitation strengthening ($\Delta\sigma_p$), which could be expressed by

Table 1 Chemical compositions of different phases in as-cast alloy by TEM−EDS measurements

Alloy	Phase	Content/at.%			
		Fe	Cr	Ni	Al
P1	Nanoprecipitate	16.72±0.2	3.50±0.1	39.02±0.3	40.74±0.2
P2	Matrix	63.52±0.7	27.86±0.4	4.98±0.1	3.62±0.1

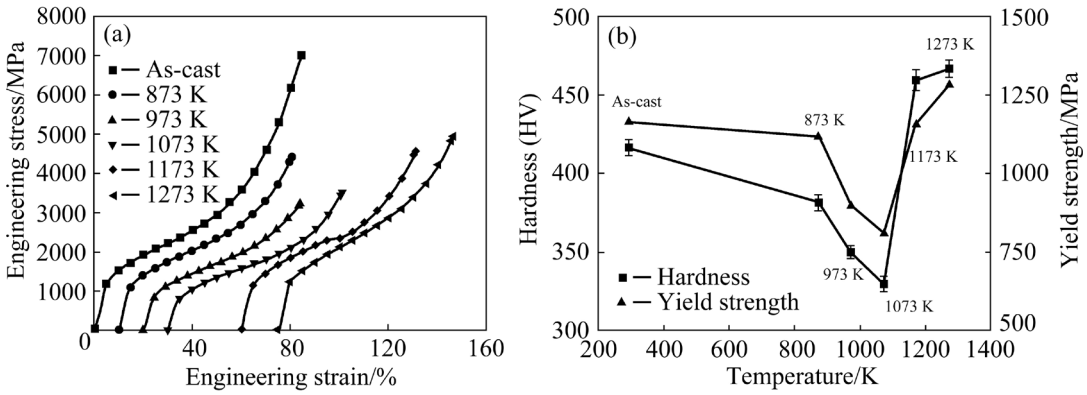

Fig. 4 Compressive stress−strain curves of $Fe_{3.5}Cr_{1.5}NiAl_{0.8}$ MCAs (a) and statistics of yield strength and hardness of $Fe_{3.5}Cr_{1.5}NiAl_{0.8}$ MCAs (b)

Table 2 Hardness and yield strength of $Fe_{3.5}Cr_{1.5}NiAl_{0.8}$ MCAs under different conditions

Heat treatment temperature/K	Hardness (HV)	Yield strength/MPa
As-cast	416.3	1164.1
873	381.4	1116.3
973	349.9	895.9
1073	329.9	809.2
1173	459.2	1155.3
1273	466.6	1281.8

the following equation [30]:

$$\sigma_y=\sigma_0+\Delta\sigma_{ss}+\Delta\sigma_{gb}+\Delta\sigma_{dis}+\Delta\sigma_p \quad (1)$$

where the value of intrinsic strength σ_0 was calculated to be 160 MPa using the rule of mixture [7]. For HEAs or MCAs, distinguishing between solute or solvent atoms was still difficult [19,31], making it hard to calculate the solid-solution strengthening. The Hall−Petch equation [32,33] could be considered as a constant method to measure grain-boundary strengthening of alloys. As the grain of the MCAs was coarse, the contribution of the grain-boundary strengthening to the yield strength was negligible.

During the process of plastic deformation, dislocations were suffered by strong diffuse obstacles, leading to the increment in strength. The dislocation density and the strength could be evaluated from Eq. (2) [7,19]:

$$\Delta\sigma_{dis}=M\alpha Gb\rho^{1/2} \quad (2)$$

where M(=2.73) is the Taylor factor of the BCC matrix [25], α(=0.33) is a constant related to materials [15], G(=83 GPa) is the shear modulus of the BCC matrix [26], b=(0.2501 nm) is the magnitude of Burgers vector of the BCC matrix, and ρ is the dislocation density. In this case, the following simple equation was applied to evaluating the dislocation density ρ:

$$\rho=2\sqrt{3}\frac{\varepsilon}{Db} \quad (3)$$

where D is the crystallite size and ε is the microstrain, and both parameters could be obtained through the Williamson−Hall method [34]. The dislocation density was determined to be $\rho=2.56\times10^{14}$ m^{-2}. Substituting these values into Eq. (2), the increased yield strength from dislocation strengthening was obtained to be 299.2 MPa. The result showed that dislocation strengthening played a significant role in the yield strength increment of the alloys.

The contribution from the precipitation hardening to the yield strength of the as-cast $Fe_{3.5}Cr_{1.5}NiAl_{0.8}$ MCA could be approximately estimated as follows. As shown in Fig. 3, the $B2$ precipitates were highly coherent with the matrix, and these NiAl-type coherent precipitates were expected to produce hardening. The precipitation hardening of a solid-solution matrix usually occurs either through the dislocation by-pass mechanism (Orowan-type) or the dislocation shearing mechanism [35]. Generally, the Orowan mechanism will occur when the size of its own precipitates is large. The yield strength increment caused by the dislocation by-pass mechanism ($\Delta\sigma_{Orowan}$) could be calculated using Eqs. (4)−(6) [36,37]:

$$\Delta\sigma_{Orowan}=M\frac{0.4Gb}{\pi\sqrt{1-\nu}}\frac{\ln(2r_m/b)}{\lambda_p} \quad (4)$$

$$r_m=\sqrt{2/3}r \quad (5)$$

$$\lambda_p=2\sqrt{2/3}r\left(\sqrt{\pi/4f}-1\right) \quad (6)$$

where ν(=0.3) is Poisson ratio [25], r(=245.509 nm) and f (=0.44) are the mean radius and the volume fraction of precipitates in the matrix, respectively, r_m and λ_p are the mean radius of the circular cross-section for the spherical precipitates and interprecipitate spacing, respectively [29].

The shearing mechanism occurred when the precipitate size was small or coherent with the solid-solution matrix, and the yield strength increment mainly resulted from three contributing factors: coherency strengthening ($\Delta\sigma_{CS}$), modulus mismatch strengthening ($\Delta\sigma_{MS}$), and order strengthening ($\Delta\sigma_{OS}$) [16]. The $\Delta\sigma_{CS}$ and $\Delta\sigma_{MS}$ made contributions before the dislocation sheared the coherent precipitate, while the $\Delta\sigma_{OS}$ occurred during shearing. The resultant yield strength increment from the coherent precipitate sheared by dislocations is the larger one between $\Delta\sigma_{CS}+\Delta\sigma_{MS}$ or $\Delta\sigma_{OS}$ [25]. When calculating the contribution of the precipitation for the yield strength by shear mechanism, the three factors were considered comprehensively because the ordered $B2$ precipitate had a good coherent relationship with the BCC matrix. Equations (7)−(9) used for calculating the yield strength increment with particle shearing mechanism are as follows [38]:

$$\Delta\sigma_{CS}=M\alpha_{\varepsilon}\left(G\varepsilon_{c}\right)^{3/2}\left(\frac{rf}{0.5Gb}\right)^{1/2} \quad (7)$$

$$\Delta\sigma_{MS}=0.0055M\left(\Delta G\right)^{3/2}\left(\frac{2f}{G}\right)^{1/2}\left(\frac{r}{b}\right)^{3m/2-1} \quad (8)$$

$$\Delta\sigma_{OS}=0.81M\frac{\gamma_{APB}}{2b}\left(\frac{3\pi f}{8}\right)^{1/2} \quad (9)$$

where α_{ε}(=2.6) is a constant for a BCC structure metals [39], m is a constant, and m=0.85 [40], ε_c(≈2/3Δα/α) is the constrained lattice misfit (ε_c≈2.8×10^{-3}), ΔG=|G−G_p| is the shear modulus mismatch between $B2$ precipitate and its matrix (G_p=80 GPa [25]), and γ_{APB} is the antiphase boundary free energy of the $B2$ precipitate phase (γ_{APB}=0.25 J/m^2 [26]). By substituting these values into Eqs. (7)−(9), the increased yield strength from dislocation shearing mechanism was obtained to be $\Delta\sigma_{CS}$=2565.5 MPa, $\Delta\sigma_{MS}$=53.4 MPa and $\Delta\sigma_{OS}$= 795.7 MPa. This result clearly demonstrated that the dislocation shearing mechanism was not applicable to $Fe_{3.5}Cr_{1.5}NiAl_{0.8}$ MCAs.

The values of $\Delta\sigma_{Orowan}$, $\Delta\sigma_{CS}$, $\Delta\sigma_{MS}$, and $\Delta\sigma_{OS}$ from Eqs. (4)−(9) are listed in Table 3. The calculated increments of the yield strength for the $B2$ precipitates from the dislocation Orowan mechanism ($\Delta\sigma_{Orowan}$) were much smaller than those from the dislocation shearing mechanism ($\Delta\sigma_{CS}$ + $\Delta\sigma_{MS}$ or $\Delta\sigma_{OS}$), implying that the Orowan mechanism was the operative mechanism for the $B2$ precipitates [19]. Thus, the resultant yield strength increment ($\Delta\sigma_p$) was 472.4 MPa for the $B2$ precipitate-strengthened BCC phase.

Table 3 Calculated increments of yield strength for $B2$ precipitates in as-cast MCAs

$\Delta\sigma_{Orowan}$/ MPa	$\Delta\sigma_{CS}$/ MPa	$\Delta\sigma_{MS}$/ MPa	$\Delta\sigma_{OS}$/ MPa	($\Delta\sigma_{CS}$+$\Delta\sigma_{MS}$)/ MPa	$\Delta\sigma_p$/ MPa
472.4	2565.5	53.4	795.7	2618.9	472.4

A bar chart directly indicating the yield strength contributions from different mechanisms according to the aforementioned results is exhibited in Fig. 5. It is apparent that there is a small discrepancy between the predicted data and the experimental values. The small discrepancy may be attributable to two factors. Firstly, the precipitates are modeled to be spherical to simplify calculations, but many of them are actually in plate-like shape. Irregular plate-shaped precipitates are anticipated to produce more resistance to plastic flow as compared to spherical precipitates [19]. Secondly, in our calculations, several intrinsic parameters (e.g., M, G, and γ_{APB}) are borrowed from BCC-based HEAs, which can to some degree affect the overall strength of the MCAs. Nevertheless, it is especially noted that the precipitation strengthening and the dislocation strengthening provide the largest strength increment.

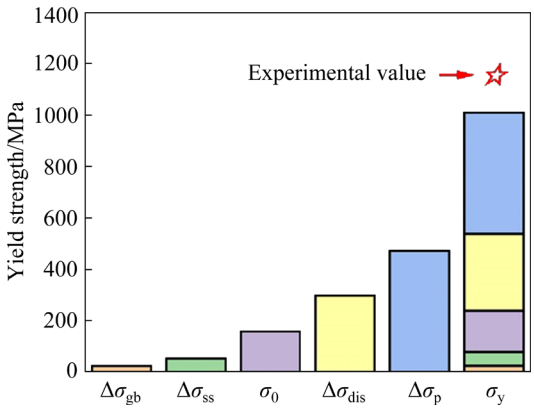

Fig. 5 Contribution of different strengthening mechanisms to yield strength in as-cast $Fe_{3.5}Cr_{1.5}NiAl_{0.8}$ MCAs

A comparison showed that the size of the precipitates increased with increasing the annealing temperature but the volume fraction decreased, clearly indicating that the precipitates grew with the increase in annealing temperature. At higher temperatures, for example, 1173 and 1273 K, the average radius of the precipitates increased significantly, indicating that they grew coarse. The calculated increments in the yield strength based on the Orowan mechanism were 220.6 and 83.9 MPa at 1173 and 1273 K, respectively. Thus, the yield strength increments obtained from the calculated precipitation strengthening were far lower than the tested values of 1155.3 and 1281.8 MPa, respectively. This discrepancy clearly demonstrated that the aforementioned Orowan mechanism was not applicable to coarse $B2$ precipitates. The load-transfer strengthening ($\Delta\sigma_{L\text{-}T}$) of the $B2$ precipitates could be assessed by the improved shear lag model as follows [41]:

$$\Delta\sigma_{L\text{-}T}=0.5\sigma_{y}fs \quad (10)$$

where f(=0.38 and 0.28) is the volume fraction of $B2$ precipitates at 1173 and 1273 K, respectively; s(=1.8 and 2.4) is the average aspect ratio of $B2$

precipitates at 1173 and 1273 K, respectively. Thus, the values of the load-transfer strengthening $\Delta\sigma_{L\text{-}T}$ at 1173 and 1273 K were estimated to be 395.1 and 430.7 MPa, respectively.

The strength enhancement in $Fe_{3.5}Cr_{1.5}NiAl_{0.8}$ MCAs was also related to the uniform distribution of *B*2 precipitates. Usually, when some of the nanoprecipitates agglomerate together to form coarse *B*2 precipitates, stress concentration will appear in the BCC matrix, which will have higher strength. The uniform distribution of *B*2 precipitates could help strengthen the matrix and facilitate a more effective load transfer at the precipitate/matrix interfaces, which could pin the mobile dislocations and suppress the dynamic recovery of the grains, subsequently increasing the probability of dislocation accumulation and propagation [42]. This was confirmed by the high yield strength of the alloys heat-treated at 1173 and 1273 K.

5 Conclusions

(1) The addition of Ni and Al elements could cause uniform dispersion of *B*2 NiAl-type coherent nanoprecipitates in a BCC-based $Fe_{3.5}Cr_{1.5}NiAl_{0.8}$ MCA. The coherent *B*2 nanoprecipitates could be maintained stable at temperatures lower than 1073 K for 2 h, with an average particle size of 245.509−251.328 nm. After the heat treatment at temperatures higher than 1173 K for 2 h, the *B*2 nanoprecipitates could be coarsened.

(2) Mechanical properties of the as-cast and heat-treated MCAs were well correlated with their microstructures, with the *B*2 coherent precipitated particles contributing to the high yield strength (809.2−1281.8 MPa) and high Vickers hardness (HV 329.9−466.6).

(3) Precipitation strengthening was the dominant strengthening mechanism, and the final yield strength increment from the Orowan mechanism was determined to be 472.4 MPa in the as-cast $Fe_{3.5}Cr_{1.5}NiAl_{0.8}$ MCA. When the heating temperature exceeded 1173 K, the load-transfer strengthening mechanism rather than the Orowan mechanism was the main contributor to the increase in the yield strength.

Acknowledgments

This work was supported by the National Natural Science Foundation of China (Nos. 52001051, U20A20278), China Postdoctoral Science Foundation (No. 2021T140082), Liaoning Revitalization Talents Program, China (No. XLYC1807047), and Major Special Project of “Scientific and Technological Innovation 2025” in Ningbo, China (No. 2019B10086).

References

[1] JIANG Sui-he, WANG Hui, WU Yuan, LIU Xiong-jun, CHEN Hong-hong, YAO Meng-ji, GAULT B, PONGE D, RAABE D, HIRATA A, CHEN Ming-wei, WANG Yan-dong, LU Zhao-ping. Ultrastrong steel via minimal lattice misfit and high-density nanoprecipitation [J]. Nature, 2017, 544: 460−464.

[2] YANG T, ZHAO Y L, LI W P, YU C Y, LUAN J H, LIN D Y, FAN L, JIAO Z B, LIU W H, LIU X J, KAI J J, HUANG J C, LIU C T. Ultrahigh-strength and ductile superlattice alloys with nanoscale disordered interfaces [J]. Science, 2020, 369: 427−432.

[3] PENG Jian, LI Zi-yong, JI Xin-bo, SUN Yan-le, FU Li-ming, SHAN Ai-dang. Decomposition kinetics of carbon-doped FeCoCrNiMn high-entropy alloy at intermediate temperature [J]. Transactions of Nonferrous Metals Society of China, 2020, 30(7): 1884−1894.

[4] CHAI Lin-jiang, XIANG Kang, XIA Ji-ying, FALLAH V, MURTY K L, YAO Zhong-wen, GAN Bin. Effects of pulsed laser surface treatments on microstructural characteristics and hardness of CrCoNi medium-entropy alloy [J]. Philosophical Magazine, 2019, 99(24): 3015−3031.

[5] GAO Yuan-kui, LIU Yong, LIU Bin, ZHANG Wei-dong, WANG Jia-wen, DU Meng. Effects of Al and Mo on high temperature oxidation behavior of refractory high entropy alloys [J]. Transactions of Nonferrous Metals Society of China, 2019, 29(7): 1476−1483.

[6] FENG Jun-jie, GAO Shuo, HAN Kun, MIAO Yi-dong, QI Ji-qiu, WEI Fu-xiang, REN Yao-jian, ZHAN Zhen-zhen, SUI Yan-wei, SUN Zhi, CAO Peng. Effect of minor B addition on microstructure and properties of $Al_{19}Co_{20}Fe_{20}Ni_{41}$ eutectic high-entropy alloy [J]. Transactions of Nonferrous Metals Society of China, 2021, 31(4): 1049−1058.

[7] WANG Ming-liang, CUI Hong-zhi, ZHAO Yu-qiao, WANG Can-ming, WEI Na, ZHAO Yong, ZHANG Xue, SONG Qiang. A simple strategy for fabrication of an FCC-based complex concentrated alloy coating with hierarchical nanoprecipitates and enhanced mechanical properties [J]. Materials & Design, 2019, 180: 107893.

[8] XU Jun, CAO Cheng-ming, GU Ping, PENG Liang-ming. Microstructures, tensile properties and serrated flow of AlCrMnFeCoNi high entropy alloys [J]. Transactions of Nonferrous Metals Society of China, 2020, 30(3): 746−755.

[9] WANG Ming-liang, LU Yi-ping, WANG Tong-min, ZHANG Chuan, CAO Zhi-qiang, LI Ting-ju, LIAW P K. A novel bulk eutectic high-entropy alloy with outstanding as-cast specific yield strengths at elevated temperatures [J]. Scripta Materialia, 2021, 204: 114132.

[10] ZHANG Guo-jia, WANG Ming-liang, LU Yi-ping, LIU De-hua, WANG Tong-min, LI Ting-ju. A novel series of $Fe_{8.25}CoCrNiMnNb_{0.1}Mo_x$ multi-component alloys with excellent combined strength and ductility [J]. Journal of Materials Engineering and Performance, 2022, 31: 5374−5381.

[11] GWALANI B, SONI V, LEE M, MANTRI S A, REN Y, BANERJEE R. Optimizing the coupled effects of Hall−Petch and precipitation strengthening in a $Al_{0.3}CoCrFeNi$ high entropy alloy [J]. Materials & Design, 2017, 121: 254−260.

[12] GAO Xu-zhou, LU Yi-ping, ZHANG Bo, LIANG Ning-ning, WU Guan-zhong, SHA Gang, LIU Ji-zi, ZHAO Yong-hao. Microstructural origins of high strength and high ductility in an $AlCoCrFeNi_{2.1}$ eutectic high-entropy alloy [J]. Acta Materialia, 2017, 141: 59−66.

[13] SONI V, GWALANI B, ALAM T, DASARI S, ZHENG Y, SENKOV O N, MIRACLE D, BANERJEE R. Phase inversion in a two-phase, BCC+*B*2, refractory high entropy alloy [J]. Acta Materialia, 2020, 185: 89−97.

[14] ZHANG Lin, SONG Ruo-kang, QU Guo-xin, LU Tong. Effect of nitrogen on microstructure and mechanical properties of $CrMnFeVTi_6$ high-entropy alloy [J]. Transactions of Nonferrous Metals Society of China, 2021, 31(8): 2415−2427.

[15] LI Chun-hui, WANG Ming-liang, ZHANG Huan-zhi, ZHANG Guo-jia, LI Tian-xin, LU Yi-ping, LI Ting-ju. A novel as-cast precipitation-strengthened $Al_{0.5}V_{0.1}FeCrMn-Ni_{0.9}$ high-entropy alloy with high strength and plasticity [J]. Science China Technological Sciences, 2021, 64(9): 1920−1926.

[16] WANG Jian-ying, FANG Jing-hua, YANG Hai-lin, LIU Zhi-lin, LI Rui-di, JI Shou-xun, WANG Yun, RUAN Jian-ming. Mechanical properties and wear resistance of medium entropy $Fe_{40}Mn_{40}Cr_{10}Co_{10}$/TiC composites [J]. Transactions of Nonferrous Metals Society of China, 2019, 29(7): 1484−1494.

[17] MING Kai-sheng, BI Xiao-fang, WANG Jian. Precipitation strengthening of ductile $Cr_{15}Fe_{20}Co_{35}Ni_{20}Mo_{10}$ alloys [J]. Scripta Materialia, 2017, 137: 88−93.

[18] KIREEVA I V, CHUMLYAKOV Y I, POBEDENNAYA Z V, VYRODOVA A V. Effect of γ'-phase particles on the orientation and temperature dependence of the mechanical behaviour of $Al_{0.3}CoCrFeNi$ high-entropy alloy single crystals [J]. Materials Science and Engineering A, 2020, 772: 138772.

[19] HE J Y, WANG H, HUANG H L, XU X D, CHEN M W, WU Y, LIU X J, NIEH T G, AN K, LU Z P. A precipitation-hardened high-entropy alloy with outstanding tensile properties [J]. Acta Materialia, 2016, 102: 187−196.

[20] SENKOV O N, ISHEIM D, SEIDMAN D N, PILCHAK A L. Development of a refractory high entropy superalloy [J]. Entropy, 2016, 18: 102.

[21] YANG Teng-fei, XIA Song-qin, LIU Shi, WANG Chen-xu, LIU Shao-shuai, ZHANG Yong, XUE Jian-ming, YAN Sha, WANG Yu-gang. Effects of Al addition on the microstructure and mechanical properties of $Al_xCoCrFeNi$ high-entropy alloys [J]. Materials Science and Engineering A, 2015, 648: 15−22.

[22] WANG Z G, ZHOU W, FU L M, WANG J F, LUO R C, HAN X C, CHEN B, WANG X D. Effect of coherent $L1_2$ nanoprecipitates on the tensile behavior of a fcc-based high-entropy alloy [J]. Materials Science and Engineering A, 2017, 696: 503−510.

[23] WANG Jun-feng, WANG Zhao-guang, WANG Xiao-dong, YANG Qi, JIN Xue-jun, WANG Li. Strengthening effect of nanoscale precipitation and transformation induced plasticity in a hot rolled copper-containing ferrite-based lightweight steel [J]. Scripta Materialia, 2017, 129: 25−29.

[24] LIANG Yao-jian, WANG Lin-jing, WEN Yu-ren, CHENG Bao-yuan, WU Qin-li, CAO Tang-qing, XIAO Qian, XUE Yun-fei, SHA Gang, WANG Yan-dong, REN Yang, LI Xiao-yan, WANG Lu, WANG Fu-chi, CAI Hong-nian. High-content ductile coherent nanoprecipitates achieve ultrastrong high-entropy alloys [J]. Nature Communications, 2018, 9: 4063.

[25] MA Yue, HAO Jia-miao, JIE Jin-chuan, WANG Qing, DONG Chuang. Coherent precipitation and strengthening in a dual-phase $AlNi_2Co_2Fe_{1.5}Cr_{1.5}$ high-entropy alloy [J]. Materials Science and Engineering A, 2019, 764: 138241.

[26] MA Yue, HAO Jia-miao, WANG Qing, ZHANG Chuan, LI Chun-ling, DONG Chuang. Temperature-affected microstructural stability of coherent cuboidal *B*2 particles in precipitation-strengthened body-centered-cubic $Al_{0.7}CoCr_2-FeNi$ high-entropy alloy [J]. Journal of Materials Science, 2019, 54: 8696−8710.

[27] LI J L, LI Z, WANG Q, DONG C, LIAW P K. Phase-field simulation of coherent BCC/*B*2 microstructures in high entropy alloys [J]. Acta Materialia, 2020, 197: 10−19.

[28] VOORHEES P W, MCFADDEN G B, JOHNSON W C. On the morphological development of second-phase particles in elastically-stressed solids [J]. Acta Metallurgica et Materialia, 1992, 40(11): 2979−2992.

[29] ZHANG J X, WANG J C, HARADA H, KOIZUMI Y. The effect of lattice misfit on the dislocation motion in superalloys during high-temperature low-stress creep [J]. Acta Materialia, 2005, 53(17): 4623−4633.

[30] SHAYSULTANOV D G, SALISHCHEV G A, IVANISENKO Y V, ZHEREBTSOV S V, TIKHONOVSKY M A, STEPANOV N D. Novel $Fe_{36}Mn_{21}Cr_{18}Ni_{15}Al_{10}$ high entropy alloy with bcc/*B*2 dual-phase structure [J]. Journal of Alloys and Compounds, 2017, 705: 756−763.

[31] PENG Han-lin, HU Ling, LI Lie-jun, GAO Ji-xiang, ZHANG Qi. On the correlation between $L1_2$ nanoparticles and mechanical properties of $(NiCo)_{52+2x}(AlTi)_{4+2x}Fe_{29-4x}Cr_{15}$ (x=0−4) high-entropy alloys [J]. Journal of Alloys and Compounds, 2020, 817: 152750.

[32] HE J Y, WANG H, WU Y, LIU X J, MAO H H, NIEH T G, LU Z P. Precipitation behavior and its effects on tensile properties of FeCoNiCr high-entropy alloys [J]. Intermetallics, 2016, 79: 41−52.

[33] HUANG Xue-ling, HUANG Lan-ping, PENG Hai-long, LIU Yong, LIU Bin, LI Song. Enhancing strength-ductility synergy in a casting non-equiatomic NiCoCr-based high-entropy alloy by Al and Ti combination addition [J]. Scripta Materialia, 2021, 200: 113898.

[34] WILLIAMSON G K, HALL W H. X-ray line broadening from filed aluminium and wolfram [J]. Acta Metallurgica,

1953, 1: 22−31.
[35] SEIDMAN D N, MARQUIS E A, DUNAND D C. Precipitation strengthening at ambient and elevated temperatures of heat-treatable Al(Sc) alloys [J]. Acta Materialia, 2002, 50: 4021−4035.
[36] ASHBY M F. Physics of strength and plasticity [M]. Cambridge: MIT Press, 1969.
[37] GRADMAN T. The physical metallurgy of microalloyed steels [M]. London: Maney Publishing, 2002.
[38] BOOTH-MORRISON C, DUNAND D C, SEIDMAN D N. Coarsening resistance at 400 ℃ of precipitation-strengthened Al−Zr−Sc−Er alloys [J]. Acta Materialia, 2011, 59: 7029−7042.
[39] GEROLD V, HABERKORN H. On the critical resolved shear stress of solid solutions containing coherent precipitates [J]. Physica Status Solidi (b), 1966, 16: 675−684.
[40] NEMBACH E. Precipitation hardening caused by a difference in shear modulus between particle and matrix [J]. Physica Status Solidi (a), 1983, 78: 571−581.
[41] NARDONE V C, PREWO K M. On the strength of discontinuous silicon carbide reinforced aluminum composites [J]. Scripta Metallurgica, 1986, 20(1): 43−48.
[42] ZHAO Yong-hao, ZHU Yun-lian, LAVERNIA E J. Strategies for improving tensile ductility of bulk nanostructured materials [J]. Advanced Engineering Materials, 2010, 12: 769−778.

BCC 基 $Fe_{3.5}Cr_{1.5}NiAl_{0.8}$ 多组元合金的显微组织稳定性与力学性能

张国家[1,2]，王明亮[1]，卢一平[1,2]，王同敏[1,2]，李廷举[1]

1. 大连理工大学 材料科学与工程学院 辽宁省凝固控制与数字化制备技术重点实验室，大连 116024；
2. 大连理工大学 材料科学与工程学院 辽宁省高熵合金材料工程研究中心，大连 116024

摘　要：研究温度对新型体心立方(BCC)基 $Fe_{3.5}Cr_{1.5}NiAl_{0.8}$ 多组元合金(MCA)中有序椭圆状 *B*2-NiAl 纳米析出相的显微组织稳定性和力学性能的影响。采用 XRD、EBSD、EPMA 和 TEM 等检测方法对该多组元合金的显微组织和物相组成进行表征。结果表明，所设计的高含量椭圆状 *B*2 纳米析出相与 BCC 基体完全共格且能在 1073 K 高温下保持稳定，平均粒径为 245.509~251.328 nm。铸态和热处理态(873 K ≤ *T* ≤ 1073 K)合金具有独特的共格结构，这是由于低错配度的共格析出强化机制可使合金具有较高的屈服强度(809.2~1164.1 MPa)。随着热处理温度的进一步提高(1173 K ≤ *T* ≤ 1273 K)，*B*2 纳米析出相的平均粒径逐渐粗化，载荷传递强化机制对其屈服强度提高起主要作用。

关键词：多组元合金；共格显微组织；显微组织演变；力学性能；强化机制

(Edited by Wei-ping CHEN)